ELSEVIER

Journal of Power Sources 93 (2001) 174–185

JOURNAL OF POWER SOURCES

www.elsevier.com/locate/jpowsour

Electrochemical study on nano-Sn, $Li_{4.4}Sn$ and $AlSi_{0.1}$ powders used as secondary lithium battery anodes

Chunsheng Wang[a,*], A. John Appleby[a], Frank E. Little[b]

[a]*Center for Electrochemical Systems and Hydrogen Research, Texas Engineering Experiment Station, Texas A and M University, College Station, Texas 77843-3402, USA*

[b]*Center for Space Power, Texas Engineering Experiment Station, Texas A and M University, College Station, Texas 77843-3118, USA*

Received 16 August 2000; accepted 23 August 2000

Abstract

It is believed that particle cracking resulting from phase transformation is responsible for the poor cycle performance of lithium alloy anodes. Pulverization effects may be reduced by using, (i) smaller active particles; (ii) active particle composites with different potentials for the onset of lithium alloy formation; and (iii) expanded alloys which have undergone a major increase during initial charging. Three alloys of the above types (nano-Sn, $AlSi_{0.1}$ and $Li_{4.4}Sn$) were studied by electrochemical impedance spectroscopy (EIS) to determine their electrochemical kinetics and intrinsic resistance during initial lithium insertion-extraction. The electrodes were prepared by sandwiching a disk of active powder between two nickel screens, so that the contact resistance may be determined by EIS and from a d.c. voltage difference across the electrode (trans-electrode voltage). A large increase in contact resistance was found during lithium discharge (extraction) from nano-Li_xSn and $Li_xAlSi_{0.1}$ alloys, compared with the small increase during the initial charge. This result suggest that the matrix materials should have a small coefficient of elasticity to give low stress on expansion of the active alloy, together with a large elastic deformation to compensate for volume reduction. This is contrary to generally accepted argument that the matrix should have a high ductility. EIS results for measurement of intrinsic resistance and reaction kinetics during initial lithium insertion into nano-Sn and $AlSi_{0.1}$ alloys show that both solid electrolyte interphase (SEI) films formed on particle surfaces, together with particle pulverization, are responsible for the high contact resistance. The electrochemical kinetics of both lithium charge and discharge are controlled by contact resistance at high states of charge.

Keywords: Lithium alloy anode; Electrochemical impedance spectroscopy; Contact resistance

1. Introduction

Lithium alloys have been extensively studied as possible replacements for carbon anodes in lithium ion batteries. The electrochemical capacities of lithium alloys may be very large (LiAl and $Li_{4.4}Sn$: 990 mA h/g, $Li_{4.4}Si$: 4200 mA h/g), compared with that of carbon (372 mA h/g). However, the large volume expansion due to existence of two phase domains (LiAl: 97% [1], $Li_{4.4}Sn$: 358% [2], $Li_{4.4}Si$: 323% [1]) results in severe particle cracking with loss of electrical contact, giving irreversible capacity losses which prevent the widespread use of such alloys in lithium batteries.

Many attempts have been made to stabilize the morphology of lithium alloy electrodes by minimizing the mechanical stress in the electrode caused by this volume expansion. Successful methods have included the following. (i) The use of composites of active and inactive materials, e.g. the so-called tin-based composite oxides (TCOs) [3], where a nano-structured active phase is dispersed either in an inert solid electrolyte or in a soft metal matrix formed on the initial charge, e.g. the system based on Sn_2Fe [4]. (ii) The use of intermetallic lithium insertion compounds, e.g. InSb [2] and Cu_6Sn_5 [5], where lithium atoms occupy interstitial sites, giving only a small volume expansion. (iii) The used of mixed active material composites (active/active composite), e.g. $SnSb_{0.14}$ [6], where stepwise lithium insertion into the different active phases buffers volume expansion. It is believed that the major volume expansion occurs during initial charging, and subsequent dealloying and alloying steps result in only small shrinkage and expansion [7]. As a result, the compound $Li_{4.4}Sn$ may have a more stable capacity during prolonged charge–discharge cycling. Initial electrochemical dealloying, followed by electrochemical

* Corresponding author. Tel.: +1-409-845-8281; fax: +1-979-845-9287.
E-mail address: cswang@pop.tamu.edu (C. Wang).

0378-7753/01/$ – see front matter
PII: S0378-7753(00)00576-0

alloying of $Li_{4.4}Sn$ prepared by melting can give useful information on the phase transformations in the Li–Sn electrode at ambient temperature.

In most case, the cracking and pulverization of the metallic host matrices is evaluated by the capacity change on charge–discharge cycling [6]. However this method cannot monitor cracking in each successive two-phase domain, with the successive single phases Sn, Li_2Sn_5, LiSn, Li_7Sn_3, Li_5Sn_2 and $Li_{22}Sn_5$. Moreover, the cycle life of the metallic electrode not only depends on cracking, but also affected by other factors. These include the stability of the solid electrolyte interphase (SEI) film on the electrode surface, the occurrence of less rapid electrochemical reaction kinetics, and the amount of active material available for reaction. Development of an in situ method to measure the pulverization of the lithium alloy electrode is important as a means of selecting suitable lithium alloy anode compositions. The conductivity measured using d.c. methods has been successfully used to measure the intrinsic resistance of graphite electrodes on insertion and extraction of lithium [8]. However, it is not applicable to lithium alloys because application of a large trans-electrode voltage affects the electrode potential, whose value is required to detect phase transformation.

In this work, Sn, $Li_{4.4}Sn$ and $AlSi_{0.1}$ powder disks sandwiched between two nickel screens were used as working electrodes. Pulverization of these alloys on cycling was monitored by the trans-electrode voltage difference when they were charged or discharged on one side only. The contact resistance and electrochemical reaction kinetics were evaluated by electrochemical impedance spectroscopy (EIS).

2. Experimental

2.1. Electrode preparation and cell description

Commercial Sn (100 nm), SnO_2 and $AlSi_{0.1}$ (8 μm) powders were purchased from Argonide Corporation, Aldrich Chemical Company, Inc., and Valimet, Inc., respectively. The $Li_{4.4}Sn$ compound was prepared by mixing the appropriate amount of Li (rod; Cypress–Foote Mineral) and Sn (powder; Aldrich) in a stainless steel crucible at 850°C for 20 min to form a molten alloy. This and all subsequent operations were conducted in a glove box, with oxygen and water vapor concentrations each less than 10 ppm. After cooling to room temperature, the $Li_{4.4}Sn$ compound was crushed and ground using a mortar to 300 mesh particle size. Electrodes were made by pressing 1:1 weight ratio $Li_{4.4}Sn$ powder (typically ca. 30 mg) and nickel powder between two nickel screen current collectors. The nano-Sn, SnO_2 and $AlSi_{0.1}$ electrodes were prepared from a mixture of 80:10:10 wt.% (or 82:8:10 wt.%) active powder, carbon black and polyvinylidene fluoride (Kynar™, Elf–Atochem), respectively. This was pressed between two nickel screen collectors using 1-methyl-2-pyrrolidinone as solvent. After drying overnight at 120°C, the electrode was pressed into a sandwich structure with a geometric surface area of 2.0 cm^2 and thickness of 1 mm. The SnO_2 electrode was used as a control.

The configuration of a typical electrode has been given previously [8]. Electrochemical measurements were conducted in a special three-electrode PTFE cell. Two lithium foils were used as both counter and reference electrodes. All potentials given are versus the Li/Li^+ reference electrode in the experimental electrolyte, which was 1.0 M lithium hexafluorophosphate ($LiPF_6$) in a 1:1:3 by volume ethylene carbonate (EC)–propylene carbonate (PC)–dimethylcarbonate (DMC) mixture (High Purity Lithium Battery Grade, Mitsubishi Chemical Company). Cells were assembled in an argon-filled glove box. Charge (lithium intercalation) and discharge (lithium extraction) was only applied on one side of the sandwich electrode in the potential-range between +0.0 and +1.5 V at constant current using an Arbin (College Station, TX) automatic battery cycler. The trans-electrode voltage between the two nickel screens was used to monitor pulverization of the electrode material during cycling.

2.2. EIS measurement

This was taken over the frequency-range 65 kHz–1.0 mHz at a potentiostatic signal amplitude of 5 mV, using a frequency response analyzer (Solartron, PRA 1250) and an electrochemical interface (Solartron, model 1286). EIS measurements were performed after fixed periods of time (4 h) during galvanostatic charging of freshly prepared lithium alloy electrodes at a 6 mA/g current. Before each measurement, the current was interrupted and the electrode was allowed to relax for 10 h with the two nickel screens connected together. The potential was recorded before each interruption of the galvanostatic current. For determination of electrochemical reaction kinetics, the signal was applied to the nickel screens connected in parallel. For intrinsic impedance measurement, the EIS was measured between the two sides.

To avoid confusion concerning the various electrode resistances discussed here, the expression intrinsic resistance is used below to refer to those physical elements of resistance which are present within the thickness of the electrode, excluding any electrochemical (Faradaic) elements. They include the electronic resistance of the series–parallel array of metal (alloy) particles themselves, the transmission line of various contact resistances between the particles, including electronic contacts with and within the binder and ionic (electrolytic) contacts, and the electronic resistances of the current collectors and the contact resistances between them and the neighboring graphite particles. This intrinsic resistance can be evaluated by above in situ EIS method.

3. Results and discussion

3.1. Initial charge–discharge behavior of lithium alloys

Fig. 1 shows the potential and trans-electrode voltage for nano-Sn, SnO_2 and $Li_{4.4}Sn$ electrodes at room temperature. The equilibrium potential of the Li–Sn system under these conditions is shown in Fig. 1c [9], the Li content being determined by the phase stoichiometry [10].

Initial Li insertion into nano-Sn shows several sloping potential plateaus (Fig. 1a) with a charge capacity of 730 mA h/g. The plateau at around 0.8 V is attributed to SEI formation on the carbon and nano-Sn powder surface, while the plateaus below 0.7 V correspond to phase transformation on Li insertion into Sn. The less prominent plateaus may be related to poor crystallinity of nano-Sn particles [6] and/or short-range ordered in lithium-rich phase structures [11].

The potential profiles for initial lithium insertion into nano-Sn in this work are similar to those obtained by Yang et al. [11] for ultrafine Sn. The trans-electrode voltage, reflecting its resistance, had a very small value (0.53 mV) before potential fell to 0.3 V. It quickly increased at this potential, which was followed by a slowly increase from 0.3 to 0.2 V, then a final decrease below 0.2 V. The behavior of this voltage indicated that the Li_xSn alloy began to pulverize at the point of phase transformation from LiSn to Li_5Sn_2 (around 0.3 V), which became more marked at the potential of $Li_{4.4}Sn$ formation. The PTFE fixture limited the expansion of electrode in thickness, but the total volume nevertheless increased due to the continued formation $Li_{4.4}Sn$ below 0.2 V. This in turn decreased the trans-electrode voltage, hence the contact resistance. A rapid increase in this voltage resulting from a reduction in electrode volume was observed during Li extraction from nano-Sn. The high contact resistance of electrode, hence loss of active material occurring during this operation, together with the charge required for SEI film formation on carbon and nano-Sn powders during initial lithium Li insertion resulted in a large irreversible capacity (390 mA h/g).

As a comparison, the electrode potential and trans-electrode voltage on initial lithium insertion into SnO_2 were also

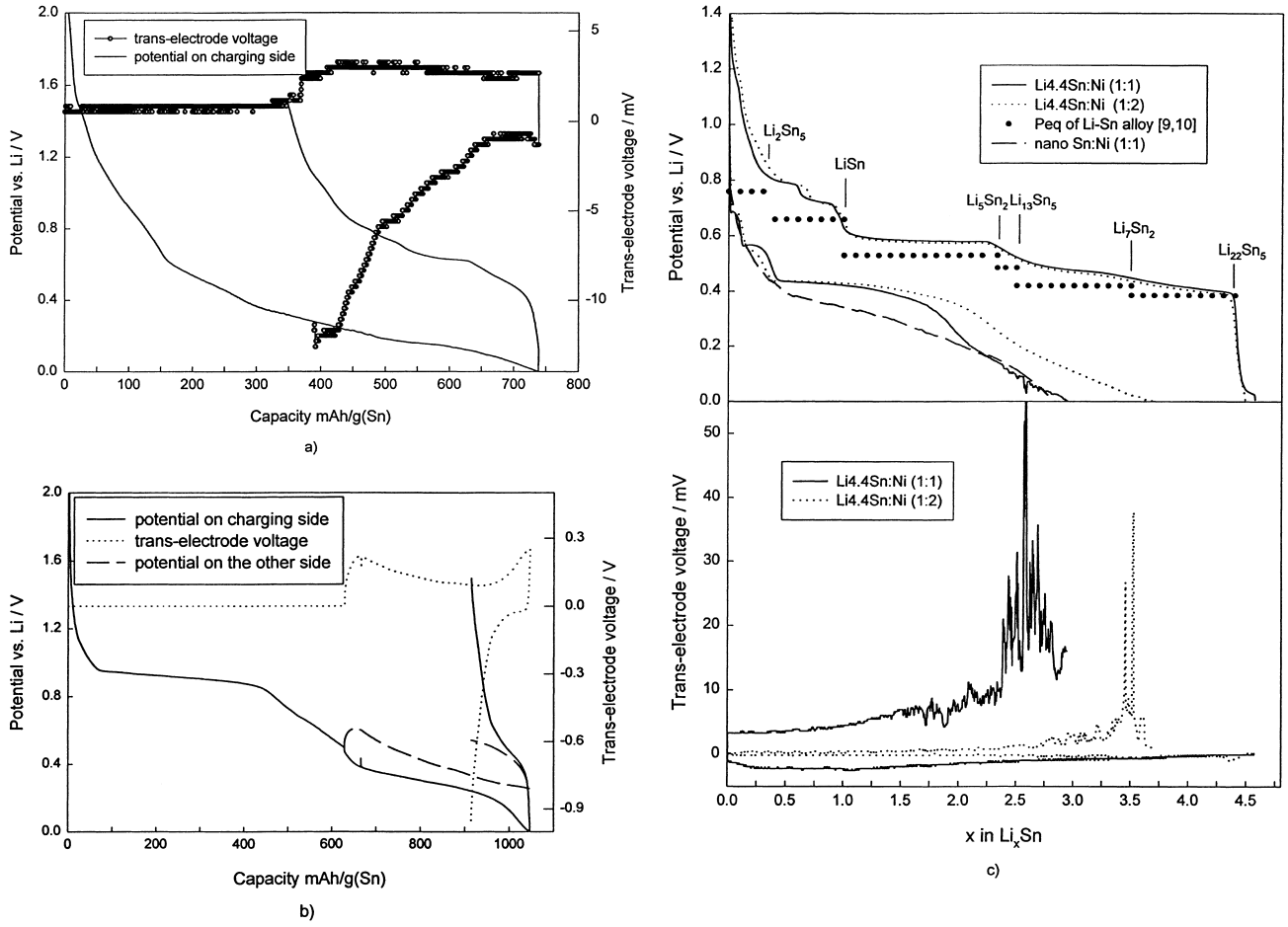

Fig. 1. Potential and trans-electrode voltage during the first charge (Li insertion) and discharge (Li extraction) cycle at 7.0 mA/g (Sn). (a) Nano-Sn containing 10 wt.% carbon, 10 wt.% PVDF; (b) SnO_2 containing 10 wt.% carbon, 10 wt.% PVDF; (c) $Li_{4.4}Sn$ and nano-Sn containing different amounts of Ni powder. The equilibrium potentials of the Li–Sn system at room temperature were taken from [9,10]. With the exception of the SnO_2 electrode, all electrodes were compressed between two PTFE holders with small holes to allow penetration of electrolyte.

investigated. Fig. 1b shows a typical potential profile for initial lithium insertion into this material [12–14], showing initial formation of Sn at around 1.0 V, followed by that of Li_xSn alloy below this potential. The small lithium reversible capacity (160 mA h/g) is due to the large thickness of the SnO_2 electrode (1 mm), which was used to prevent the contact of the two Ni meshes on each side during compression. The low trans-electrode voltage showed that the contact resistance is small and stable during the electrochemical reaction of lithium with SnO_2 to give Sn and Li_2O, and during Li insertion into Sn at above 0.5 V. The rapid increase in trans-electrode voltage at around 0.5 V in Fig. 1b suggests that pulverization of Li_xSn particles occurred and became more pronounced on further lithium insertion. The decrease in contact resistance in the potential-range 0.4–0.2 V may be attributed to compression resulting from volume expansion during Li insertion into Sn. The final increase in contact resistance may be due to cracking of the Li_2O matrix [15], caused by either formation of $Li_{4.4}Sn$ or by UPD of Li on $Li_{4.4}Sn$ alloy [16]. Similar to nano-Sn, the contact resistance of SnO_2 electrode increased very rapidly during Li extraction due to the shrinkage of the Li_xSn alloy formed.

To compare the phase transformations on Li_xSn formed by electrochemistry and melt methods, the potential and trans-electrode voltage during initial electrochemical Li extraction and insertion from $Li_{4.4}Sn$ prepared from a melt were studied as shown in Fig. 1c. The open-circuit potential of the electrode after assembly was around 5 mV versus Li, which is much lower than the equilibrium potential (0.38 V) of $Li_{4.4}Sn$. Some lithium was therefore present on the $Li_{4.4}Sn$ surface. Initial discharge (Li extraction) removed the Li coating, so that the electrode rapidly attained the 0.38 V equilibrium potential. The Li extraction potential profiles for two $Li_{4.4}Sn$ electrodes clearly show a two-phase region whose potential was very close to the equilibrium value reported by Huggins [9] and Winter et al. [10]. However, during subsequent Li insertion, the potential plateau of the Li-rich phase disappeared, and the overpotential (i.e. the difference between equilibrium potential and the Li insertion potential) increased with increasing x in Li_xSn. Increasing the content of nickel powder current collector improved the conductivity of electrode, and enhanced the capacity lithium insertion after its extraction from the $Li_{4.4}Sn$ electrode. However, the potential plateau resulting from the Li-rich phase transformation was still not observed. The Li insertion potential for melt-prepared $Li_{4.4}Sn$ after Li extraction is therefore similar to the initial Li insertion into ultrafine Sn (0.8 μm) reported by Yang [6]. The most reasonable explanation for the potential profile of this $Li_{4.4}Sn$ electrode is that the high stresses resulting from the Li-rich phase transformation limit the formation of long-range ordered Li_xSn structures ($4.4 > x > 2.5$), even for preformed $Li_{4.4}Sn$ with long-range order. Short-range order in Sn, and the crystalline structure of $Li_{4.4}Sn$ prepared by ambient temperature electrochemical methods, have been confirmed by X-ray diffraction [11] and X-ray absorption measurements [17]. The presence of potential plateaus for Sn, Li_2Sn_5 and LiSn during Li insertion results from the relatively small volume expansion of their related structures [12]. The long-range order of the melt-preparation $Li_{4.4}Sn$ was not helpful in giving an ordered crystalline structure during later electrochemical Li insertion. Fig. 1c also show a gradual increases in overpotential with the Li extraction from Li_xSn and with the fraction of newly formed phase. The first was due to a smaller degree of contact between active particles resulting from the reduction in volume, as indicated by the change in trans-electrode voltage. The overpotential during each phase transformation resulted from Li diffusion [8].

Another significant observation from Fig. 1c is that lithium may show UPD on the Sn surface at potentials near 0.0 V, because the increasing trans-electrode voltage began to decrease at this potential. UPD above 0.0 V was confirmed by the use of high-resolution transmission electron microscopy (HETEM) to examine nanometer-scale SnO_2 after Li insertion to 0.0 V. [16] and by electrochemical charge–discharge on a SnO_2 anode [18].

The trans-electrode voltage versus the Li content of nano-Sn and $Li_{4.4}Sn$ electrodes shown in Fig. 1 were replotted as trans-electrode voltage versus potential because the phase transformation was potential-dependent (Fig. 2). The trans-electrode voltage of the nano-Sn and $Li_{4.4}Sn$ electrodes show similar behavior, i.e. a small increase during initial Li extraction from $Li_{4.4}Sn$ or initial Li insertion into nano-Sn, and a rapid increase during Li insertion into dealloyed $Li_{4.4}Sn$ or Li extraction from lithiated Sn. The small increase in trans-electrode voltage during initial Li extraction from $Li_{4.4}Sn$, and the large increase during later Li insertion into dealloyed $Li_{4.4}Sn$, resulted from the compressive stress from the PTFE holder. This compensated for the volume reduction of Li_xSn, but induced a high degree of pulverization during later Li insertion. Application of high pressure on a

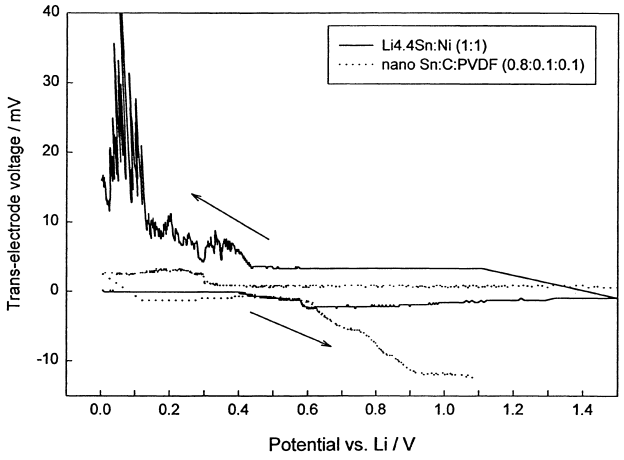

Fig. 2. The trans-electrode voltages across nano-Sn and $Li_{4.4}Sn$ during initial charge–discharge at different potentials. Electrodes compressed as in Fig. 1.

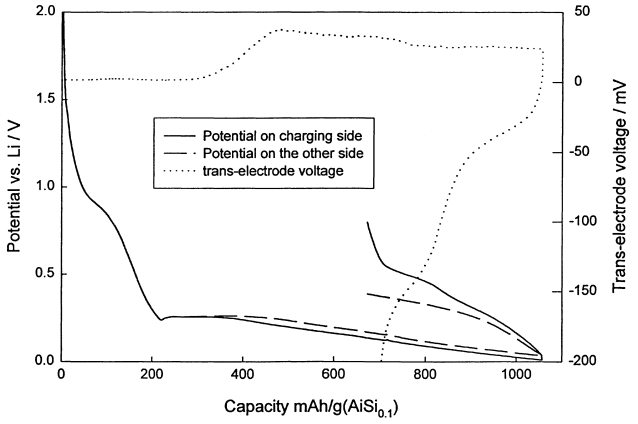

Fig. 3. Potential and trans-electrode voltage during first charge–discharge cycle at 7.0 mA/g for $AlSi_{0.1}$ electrode containing 15 wt.% carbon, 10 wt.% PVDF.

nano-Sn electrode via the PTFE holder and volume expansion during initial Li insertion caused plastic deformation of the carbon, so effective contact between Sn particles was not recovered on shrinkage during Li extraction, as the high trans-electrode voltage indicated. The results in Fig. 2 suggest that, (i) assembly in the expanded state electrode is not helpful in improve the charge stability of Sn electrodes; (ii) the matrix materials should have a coefficient of elasticity but a large elastic deformation region because a low coefficient of elasticity can decrease stress induced by volume expansion during Li insertion and a large elastic deformation of the matrix can compensate the shrinkage of active particles during Li extraction. This is contradictory to the generally accepted concept that the matrix should have high ductility.

The behavior of the trans-electrode voltage on an $AlSi_{0.1}$ electrode (Fig. 3) differs from that on nano-Sn. There are two less prominent voltage peaks in the $AlSi_{0.1}$ electrode, which may result from the different Li insertion potentials of Al and Si, which will discussed more detail in next section. The important feature in the potential profile in Fig. 3 is the existence of a nucleation barrier, which gives a rising potential during Li insertion [9]. Similar potential profiles are also seen in Al [18] and Sn–Si electrodes [9]. A higher voltage across the $AlSi_{0.1}$ electrode compared with that of the corresponding nano-Sn is due to the larger particles and a lack of compression in case of $AlSi_{0.1}$.

3.2. EIS characteristics of nano-Sn and $AlSi_{0.1}$ electrodes

Fig. 4 shows the potential measured at the end of each charge current pulse (4 h, corresponding to 24 mA h/g) and the characteristic frequency (f^*) as a function of charge capacity. The characteristic frequency is defined by the frequency at the highest imaginary point of each semicircle. After 10 h relaxation time between each current pulse, the EIS to determine the kinetic and intrinsic impedance for lithium insertion and extraction were obtained (Fig. 5). Fig. 6 shows selected Nyquist plots for the reaction kinetic and intrinsic impedances at the Li insertion levels specified in Fig. 4. The Li insertion capacity into nano-Sn below 0.8 V measured using pulsed charging (Fig. 4) was smaller than that obtained using continuous galvanostatic charging (Fig. 1). In contrast, the measured capacities above 0.8 V for the formation of the SEI film on active material and carbon powder surfaces were the inverse of the above for the two techniques. This difference may be explained by the long total galvanostatic charging time, which favors growth of the SEI film, as in cases where low charge current are used [8], together with the pulverization of Sn particles, as is indicated by the high trans-electrode voltage (compare Figs. 1 and 4). The small potential plateau about 1.0 V (C–D) may be result some of the Sn oxidizing to SnO_2 during overnight drying at 120°C, with SnO_2 conversion to Sn on Li insertion ($SnO_2 + 4Li^+ + 4e \rightarrow 2LiO + Sn$). Figs. 5a and 6a show that the Nyquist plots for kinetic Li insertion–extraction at the open-circuit potential contain depressed semicircles in the high frequency region with an inclined line at low frequencies, as in $SnSb_{0.14}$ [6]. On Li insertion, the depressed semicircles first increase in diameter, and then begin to decrease after point E, when a new depressed semicircle appears in the middle frequency region (Fig. 6a). The initial increase in diameter may result from the increase in contact, SEI film, and charge transfer resistances. In contrast to their change in diameter, the characteristic frequencies (f_k^*) of the first depressed semicircles first decrease, and then begin to increase after point D (Fig. 4). A possible reason for all of the above changes is that a depressed semicircle corresponding to charge transfer is mingled with the first SEI semicircle, but moves to the low-frequency region on Li insertion, with separation of the two at low potentials. A movement of the charge transfer semicircle to the low frequency region has also been reported during initial Li insertion into graphite [19]. The suddenly decrease in both trans-electrode voltage and in characteristic frequency f_k^* near 0.0 V (Fig. 4) may be due to UPD of Li on the Sn particle surface. Besides the trans-electrode voltage of nano-Sn, the growth of SEI film and active material pulverization on initial Li insertion can also be monitored by the intrinsic impedance, as shown in Figs. 5b and 6b. The overall structure of the Nyquist plot for the intrinsic impedance consists of two depressed semicircles. The first high frequency semicircle has been attributed to the contact resistance between Sn particles and the current collector, with the second semicircle in the low frequency region resulting from the particle-to-particle contact resistance [8]. On Li insertion, the diameters of both depressed semicircles increase, but more rapidly for the second semicircle than that for the first, so the system becomes a small semicircle plus a inclined line at the low potentials (Fig. 6b). The small second semicircle and the inclined line overlap at potentials close to 0.0 V. The behavior of the intrinsic impedance can be explained by an increase of contact resistance due to the growth of the

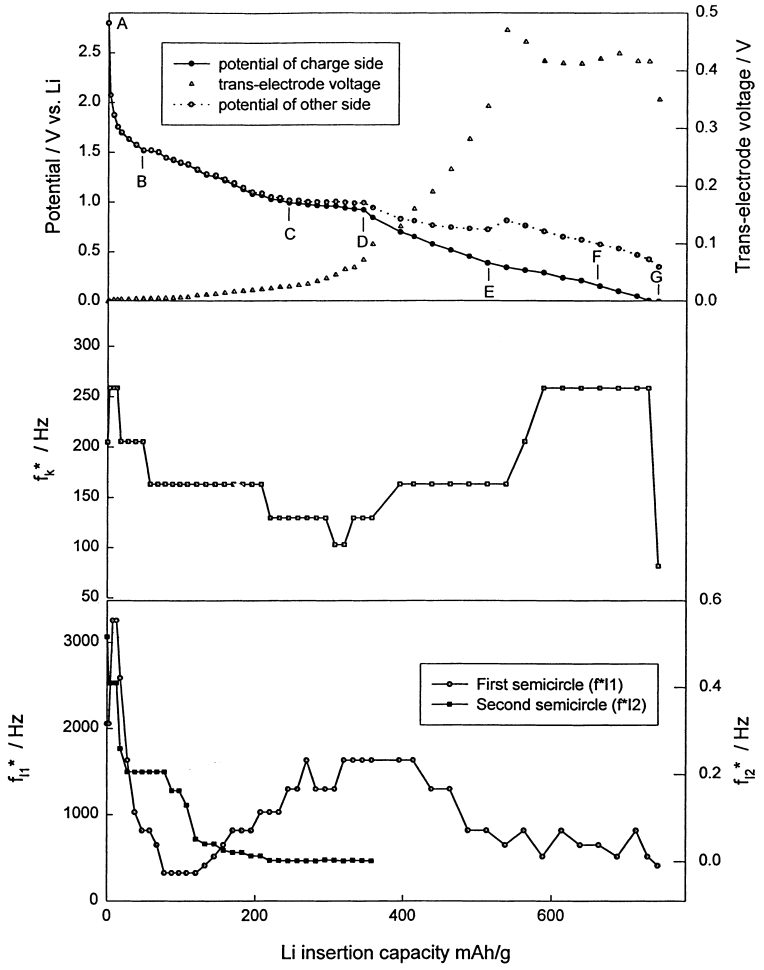

Fig. 4. The potential and characteristic frequency for the kinetic (f_k^*) and intrinsic impedance (f_I^*) of a nano-Sn electrode as a function of the initial Li insertion capacity. f_{I1}^* and f_{I2}^* are the respective characteristic frequencies the first and second semicircle of the intrinsic impedance. Potentials were measured at the end of current pulses (6 mA/g for 4 h). After 10 h relaxation at each point, EIS measurements for intrinsic and reaction resistance were taken.

SEI film on Sn and carbon point D, and by pulverization of Sn particles after point D. Finally, the electrode broke up after point E. A more detailed explanation is given below.

During intrinsic impedance measurement, a sinusoidal voltage signal (±5 mV) applied between the two sides of the electrode will result in similar lithium insertion and extraction behavior into Sn particles at each side. The quantity of electrochemically-active Sn particles on each side will increase with increase in particle-to-particle contact resistance. When pulverization of active material results in fracture of the electrode, the intrinsic impedance becomes equivalent to the kinetic impedance of a cell with one half of the electrode acting as anode and the other half as a cathode, and the particle-to-particle contact resistance within each part becomes small. Therefore, similar to the kinetic impedance, the first high frequency semicircle for the intrinsic impedance of a fractured electrode may be attributed to the contact resistance between the particles and the current collector combined with the SEI film resistance. The second semicircle in the middle frequency-range then corresponds to the particle-to-particle contact resistance combined with the charge transfer resistance. The sloping line in the low frequency region may be attributed to Li diffusion. The slow decrease in the second semicircle diameter after the electrode fractures may result from an improvement in conductivity induced by volume expansion during further Li insertion into Sn particles. If this explanation is correct, and if the electrode fractures exactly down its center, the intrinsic impedance spectrum of such an electrode should be similar to its kinetic impedance spectrum. The ±5 mV sinusoidal voltage signal applied across the Sn electrode to measure intrinsic impedance results in a ±2.5 mV change to the Li reference on each side of the electrode. This gives 50% of the current generated in equivalent kinetic impedance measurements from one half of the total Sn particles acting either as an anode or as a cathode. Fig. 7 shows the comparison of intrinsic impedance with kinetic impedance at potentials 10 mV and 0.0 V. The similarity of the two confirms the above explanation, and the small difference noted may result from the fact that the electrode is not fractured exactly down the center.

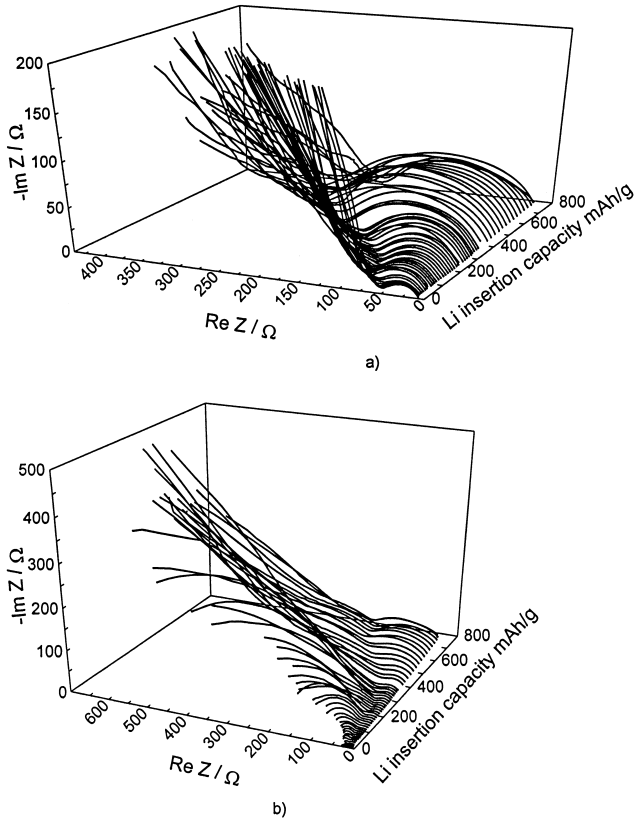

Fig. 5. Nyquist plots for (a) reaction kinetics and (b) intrinsic impedance measured at different intercalation levels during initial Li insertion into a nano-Sn anode.

Growth of the SEI film and particle pulverization also can be seen from the change in the characteristic frequency of the first semicircles in measurement of intrinsic impedance (Fig. 4). Film growth from potential B to point D decreases the contact capacitance, leading a decrease in RC (the inverse of the characteristic frequency) while resistance increases in this region. However particle pulverization after point increases the overall surface area, resulting in a increase in contact capacitance and contact resistance, thus decreasing the characteristic frequency as shown in Fig. 4. The continued decrease in the characteristic frequency of the second semicircle due to an increase in particle-to-particle contact resistance before point D occurs because this happens more rapidly than the decrease of capacitance, leading to an increases in the value of RC.

About 25% of the intrinsic impedance of the electrode is in series with its kinetic impedance [19], and the characteristic frequency of the first semicircle in the kinetic impedance lies between that of the first and second semicircles in the intrinsic impedance. Hence, 25% of the total contact, SEI film, and charge transfer impedances at low Li insertion levels should be contained within the first semicircle for the kinetic impedance.

The kinetic and intrinsic resistance of a compressed $AlSi_{0.1}$ electrode was also investigated by EIS. Fig. 8 shows the potential measured at the end of each charge current pulse (4 h, corresponding to 18 mA h/g) and the characteristic frequency (f^*) as a function of charge capacity. After 10 h of relaxation time between each current pulse, the EIS for lithium insertion–extraction kinetic and intrinsic impedance was measured as shown in Fig. 9. The potential profile for the compressed $AlSi_{0.1}$ electrode during pulsed charging (Fig. 8) was similar to the potential change of the same electrode without compression under continuous galvanostatic charging (Fig. 3), except for changes resulting from a smaller capacity. The small capacity above 0.4 V was due to the small amount of carbon (8 wt.%) and that below 0.4 V was attributed to further time-dependent alloy pulverization during the long relaxation time [6]. The trans-electrode voltage for $AlSi_{0.1}$ shows three peaks at different Li insertion levels. From the equilibrium Al–Si phase diagram [21], $AlSi_{0.1}$ alloy consists of two Al and Si phases. The potential for initial Li insertion into Al at around 0.39 V [20] was somewhat higher than the value of 0.34 V [9] for Si. It is reasonable to attribute the first voltage peak at high potential to pulverization of LiAl, the second peak at low potentials to pulverization of $Li_{1.7}Si$, and the third voltage peak at 0.0 V to pulverization of both compounds. The decrease in trans-electrode voltage after each peak may be due to higher conductivity resulting from volume expansion during Li insertion and from compression by the PTFE holder. The electrode kinetic Nyquist plots for $AlSi_{0.1}$ shows a depressed semicircle in the high frequency region and an inclined line at low frequencies, together with a continuous increase in semicircle diameter as a function of Li content. In contrast to nano-Sn, no second semicircle appears even at high Li content, and no characteristic frequency shift to the low frequency region occurs. This suggests that with this electrode, the semicircle characteristic of the charge transfer reaction is still mingled in the first semicircle even at 0.0 V. The diameters of the two depressed semicircle in the intrinsic impedance change with Li content in a same way as the trans-electrode voltage, giving a maximum impedance when the voltage is greatest. The change in the characteristic frequency for the first semicircle in the intrinsic impedance at different Li contents was inversely related to the changes in trans-electrode voltage (Fig. 8). This phenomenon appears to be related to alloy particle pulverization, i.e. this increases the contact resistance (R) and the surface area, increasing both the trans-electrode voltage and the contact capacitance (C), which together decrease the characteristic frequency. The volume expansion resulting from further Li insertion improved the conductivity of the compressed electrode, which decreased the contact resistance and capacitance, leading to both an increase in characteristic frequency and a decreased trans-electrode voltage. The characteristic frequency of the first semicircle in the intrinsic impedance was higher than that in the kinetic impedance (Fig. 8), suggesting that the part of the contact impedance is mingled with the semicircle corresponding to the kinetic impedance. To compare the trans-electrode voltage with the

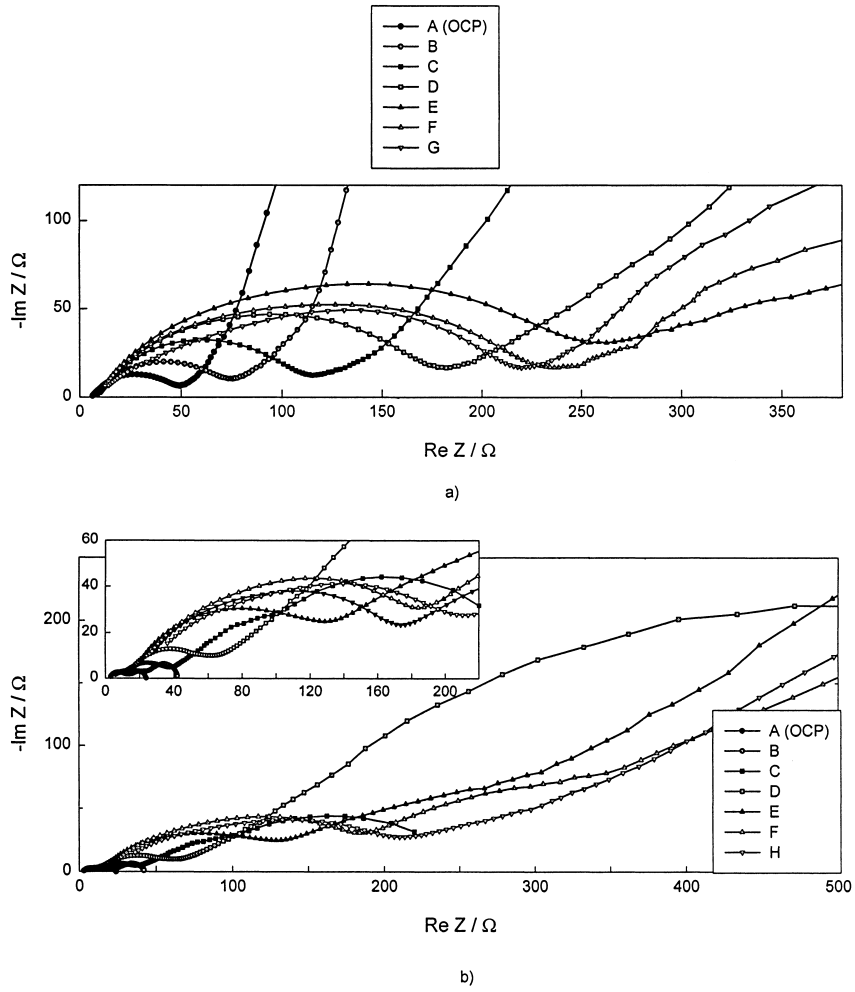

Fig. 6. The selected impedance from Fig. 5 at the Li insertion levels specified in Fig. 4. (a) Kinetic impedance selected from Fig. 5(a); (b) intrinsic impedance selected from Fig. 5b.

contact resistance and to analyze the influence of contact resistance on kinetic resistance, the kinetic and intrinsic impedances of $AlSi_{0.1}$ at the Li contents E–J showing maximum or minimum trans-electrode values in Fig. 8 are shown in Fig. 10. The impedances where the potential shows a minimum are also shown to examine the influence of nucleation on kinetic and intrinsic resistance.

The abnormal increase in potential during Li insertion into Al or Si alloy has usually attributed to nucleation of the lithated alloy phase [9], not to fragmentation of an oxide film on the $AlSi_{0.1}$ particle surface, since the potential increase reappeared during subsequent charge–discharge cycles. The change in contact resistance follows that in the potential during Li insertion, decreasing from point A to B, and beginning to increase after point B (Fig. 10b). Volume expansion during LiAl phase nucleation was responsible for the initial decrease in contact resistance (A–B), and the subsequent pulverization of LiAl increased the contact

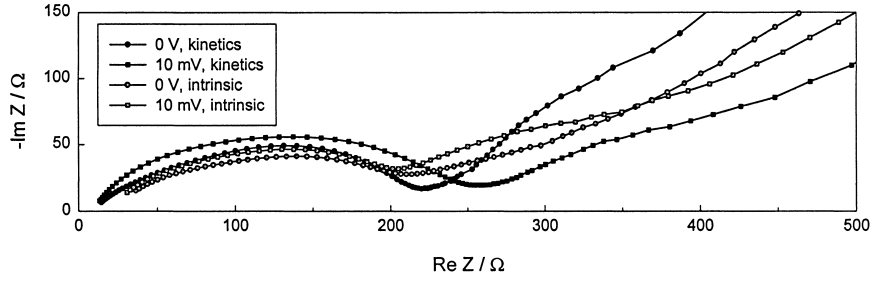

Fig. 7. Comparison of kinetic and intrinsic impedance of a nano-Sn electrode at 10 and 0.0 mV.

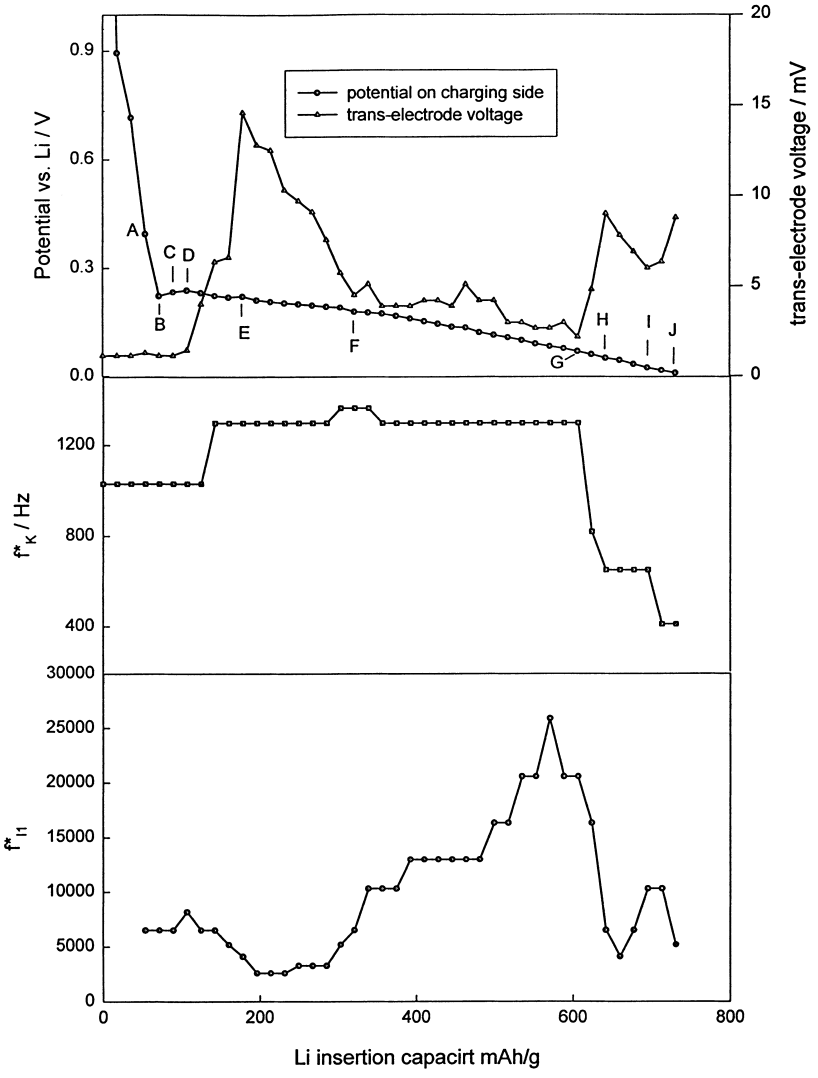

Fig. 8. The potential and characteristic frequency for the kinetic (f_k^*) and intrinsic impedance (f_I^*) as a function of initial Li insertion capacity for an $AlSi_{0.1}$ electrode containing 8 wt.% carbon, 10 wt.% PVDF, and compressed as in Fig. 1. f_{I1}^* is the characteristic frequency for the first semicircle of the intrinsic impedance. Potentials were measured at the end of current pulses (4.5 mA/g for 4 h). EIS measurements taken as in Fig. 4.

resistance. The potential profile in this region shows that the reaction resistance at point B should have a highest value because the potential profile in Fig. 8 shows the highest overpotential at point B. However the kinetic Nyquist plot shows an initial increase in resistance from point A to B, and then stability from point B to C, finally increasing again from point C to D in Fig. 10a. This phenomenon appears to be a time-dependent process related to an increase in resistance during the 10 h of relaxation time, e.g. pulverization and SEI film formation on active particles. This resistance increase should gradually become slower with time if no particle pulverization occur (as does SEI formation on Li metal) and become higher with active particle pulverization. For the same reason the kinetic impedance increases from point E to F in Fig. 10a, although the intrinsic resistance decreases in the same region (Fig. 10b), and the kinetic resistance follows the intrinsic resistance after Li insertion for long periods of time (from point G to J). Therefore, the contact resistance controls the kinetic resistance at high Li content, as in the nano-Sn electrode. A time dependent increase in impedance has also been seen in $Li_xSnSb_{0.14}$ composite electrode stored in 1 M $LiClO_4$/PC + DME and 1 M $LiClO_4$/PC solutions [6].

Another observation from Fig. 8 is the voltage increase at around 0.0 V, which suggests that pulverization of the alloy is more marked at high Li content. To investigate this effect, the $AlSi_{0.1}$ electrode was short-circuited to the Li counter electrode for 20 min and for 1 h after it being pulse charged to 0 V in both cases. After 10 h relaxation time, kinetic and intrinsic EIS were measured (Fig. 11). Compared with Figs. 10 and 11, both kinetic and intrinsic resistance quickly increased, especially the latter. A semicircle in the high frequency region and a line in low frequencies in the intrinsic impedance suggests that the $AlSi_{0.1}$ electrode

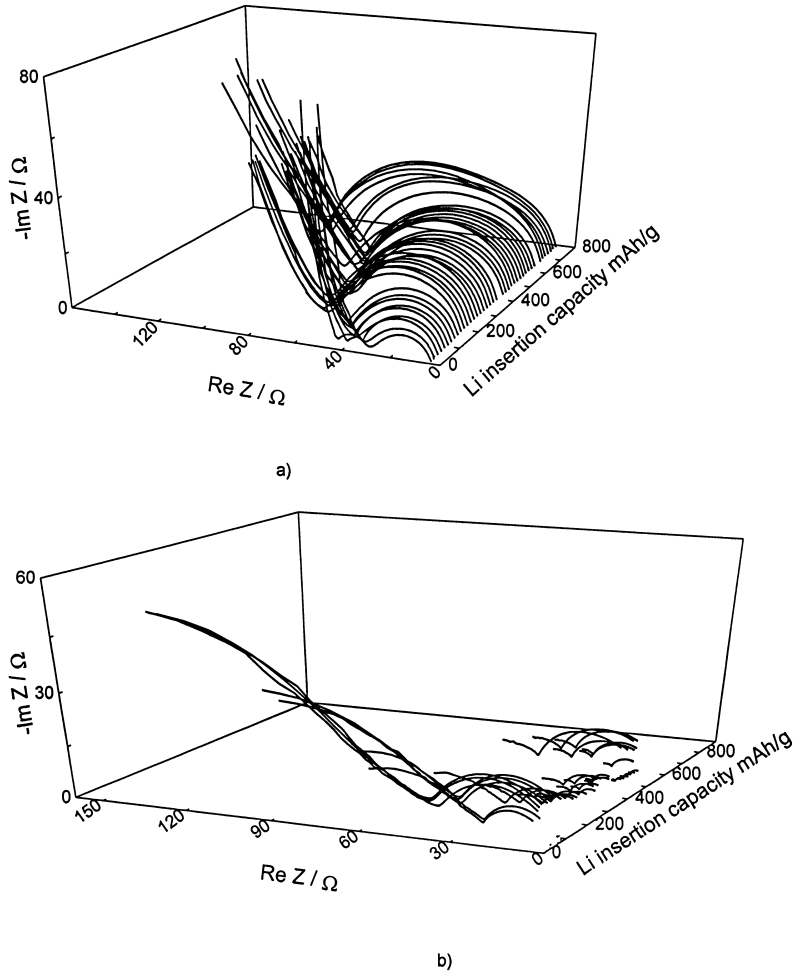

Fig. 9. Nyquist plots for (a) reaction kinetics and (b) intrinsic impedance measured at different intercalation levels during initial Li insertion into a compressed $AlSi_{0.1}$ anode.

was fractured after being short-circuited for 20 min (Fig. 11). A slightly smaller intrinsic impedance semicircle diameter than that in the kinetic impedance may attributed to the electrode not being fractured into two halves, so the intrinsic impedance was most that for the part of the electrode with the less active alloy. Comparing the trans-electrode voltage at different Li contents in Fig. 8 with the intrinsic impedance in Fig. 10b, it is seen that they both change in the same way. Therefore the trans-electrode voltage difference can be used to monitor the contact resistance of the lithium alloy electrode during charge–discharge cycling.

3.3. The methods to improve the cycling stability of lithium alloy electrode

Besenhard et al. [10] believed that the major increase in volume occurs only in the first alloying half cycle of lithium alloy electrodes, and shrinkage and expansion during subsequent dealloying and alloying are small. However the expanded $Li_{4.4}Sn$ electrode did not show high capacity retention on cycling. The potential profile and trans-electrode voltage during subsequent Li insertion into dealloyed $Li_{4.4}Sn$ were similar to those for initial Li insertion into the nano-Sn electrode (Figs. 1 and 2). Significant advantages in using ultra-small active particles [6] or a multiphase structure with active material in a supporting conductive matrix [22] have been reported. However, the capacity retention of such electrodes (e.g. nano-Sn and $AlSi_{0.1}$ alloy) is still insufficient [10], and their kinetic resistance is still controlled by contact resistance at high Li content. Wolfenstine et al. [23] believed that decreasing the Sn particle or grain size will not alone solve the mechanical instability problem, because their theoretical and experimental data revealed that only a Sn grain below that of the unit cell size can prevent fracture. Since the crystal structure of $Li_{4.4}Sn$ formed electrochemically differs somewhat from that of their melt preparation, the critical grain size may also be different from their suggested value. The amount of Li irreversibly consumed in SEI formation also increases with decrease of Sn particle size. An Sn-based amorphous composite oxide, in which a nano-structured active phase is highly dispersed

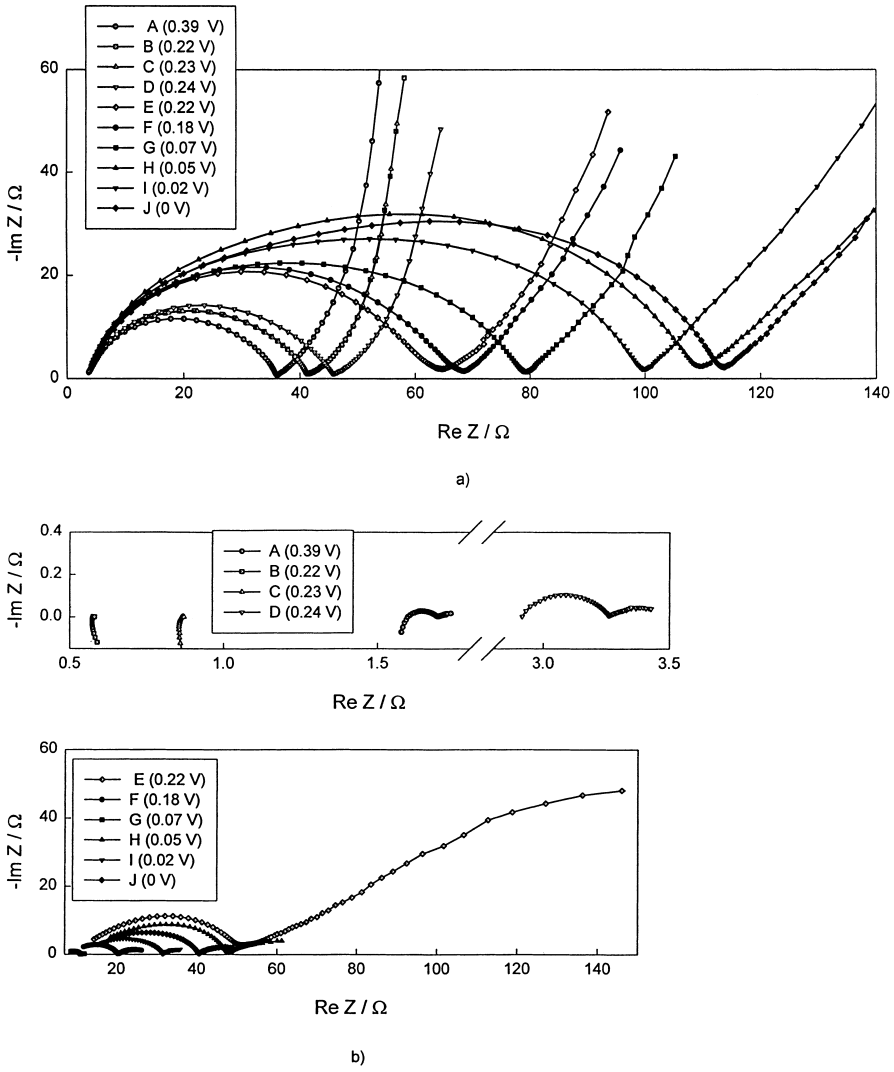

Fig. 10. The selected impedance from Fig. 9 at the Li insertion levels specified in Fig. 8. (a) Kinetic impedance selected from Fig. 9(a); (b) intrinsic impedance selected from Fig. 9b.

in an inert glassy material with mixed conduction proved successful [3]. However, continued aggregation of Sn atoms into clusters during charge–discharge cycling decreases the charge retention of the SnO-based composite electrode [24], because its equilibrium phase structure consists of Sn particles dispersed in a Li_2O-based matrix. A possible way to reduce aggregation of Sn atoms is to use a electrode alloy in which Sn is dissolved in the conducing matrix as a solid solution. One such example is Fe–Si, in which 15 wt.% of Si dissolves in Fe at room temperature. However in our experi-

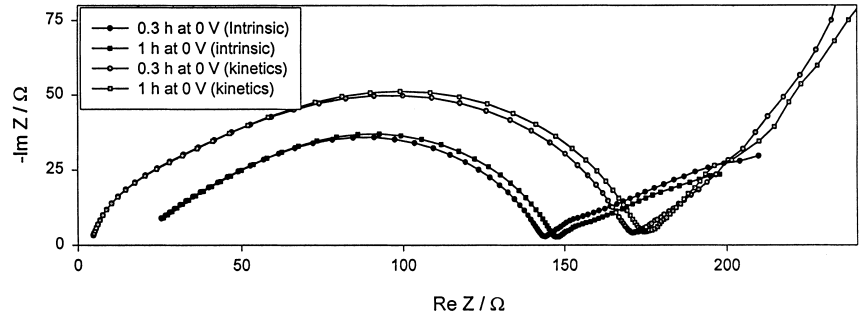

Fig. 11. Comparison of kinetic and intrinsic impedance of a $AlSi_{0.1}$ electrode, which was short-circuited to the Li counter electrode for 20 min and for 1 h after it being pulse charged to 0 V in both cases electrode at 10 and 0.0 mV.

ments, no capacity for Li insertion into Fe-15 wt.% Si has been observed, even for very low cycling currents (1 mA/g). These results suggest that individual Sn atoms dissolved in the matrix cannot absorb Li, although Li can be inserted into Sn clusters. Because the volume change for solid solution formation is generally less than that for phase transformation, an alternative way of solving the problem of high volume expansion is to select a metal or alloy which can form an Li solid solution over a large Li composition-range.

4. Conclusion

EIS has been applied to nano-Sn and $AlSi_{0.1}$ electrodes sandwiched between nickel screen current collectors to investigate the influence of contact resistance on kinetic resistance during initial lithium insertion. Application of a trans-electrode voltage was used to monitor contact resistance during the first Li insertion–extraction cycle. The value obtained was compared with the contact resistance determined by EIS. The increase in contact resistance during initial Li insertion into the alloy electrode resulted from the presence of the SEI film and because of alloy pulverization. The new area formed by pulverization in turn enhanced the irreversible capacity for SEI formation. At a high degree of Li insertion, the electrochemical reaction kinetics mainly depended on the contact resistance of the electrode. The behavior of the trans-electrode voltage across nano-Sn, $AlSi_{0.1}$ and $Li_{4.4}Sn$ during the first charge–discharge cycle suggests that the binder or matrix material in the electrode should have a low coefficient of elasticity to reduce the stress induced by volume expansion. It should also have a high elastic deformation to compensate for the shrinkage of active particles during Li extraction. This is contradictory to generally accepted opinion that the matrix should have a high ductility.

Acknowledgements

We gratefully acknowledge NASA-Glenn Research Center, Cleveland OH, for support of this work.

References

[1] D. Fauteux, R. Koksbang, J. Appl. Electrochem. 23 (1993) 1.
[2] J.T. Vaughey, J. O'Hara, M.M. Thackeray, Electrochem. Solid State Lett. 3 (2000) 13.
[3] Y. Idota, T. Kubota, A. Matsufuji, Y. Maekawa, T. Miyasaka, Science 276 (1997) 1395.
[4] O. Mao, R.A. Dunlap, J.R. Dahn, J. Electrochem. Soc. 146 (1999) 405.
[5] K.D. Kepler, J.T. Vaughey, M.M. Thackeray, Electrochem. Solid State Lett. 2 (1999) 307.
[6] J. Yang, Y. Takeda, N. Imanishi, O. Yamamoto, J. Electrochem. Soc. 146 (1999) 4009.
[7] J.O. Besenhard, J. Yang, M. Winter, J. Power Sources 68 (1997) 87.
[8] C. Wang, I. Kakwan, A.J. Appleby, F.E. Little, J. Electroanal. Chem. 489 (2000) 55.
[9] R.A. Huggins, J. Power Sources 81-82 (1999) 13.
[10] M. Winter, J.O. Besenhard, Electrochim. Acta 45 (1999) 31.
[11] J.R. Dahn, I.A. Courtney, O. Mao, Solid State Ionics 111 (1998) 289.
[12] I.A. Courtney, J.R. Dahn, J. Electrochem. Soc. 144 (1997) 2045.
[13] J. Morales, L. Sanchez, J. Electrochem. Soc. 146 (1999) 1640.
[14] W. Liu, X. Huang, Z. Wang, H. Li, L. Chen, J. Eletrochem. Soc. 145 (1998) 59.
[15] I.A. Courtney, J.R. Dahn, J. Electrochem. Soc. 144 (1997) 2943.
[16] H. Li, X. Huang, L. Chen, Electrochem. Solid State Lett. 1 (1998) 241.
[17] A.N. Mansour, S. Mukerjee, X.Q. Yang, J. McBreen, J. Electrochem. Soc. 147 (2000) 869.
[18] A.S. Baranski, W.R. Fowcett, J. Eletrochem. Soc. 129 (1982) 901.
[19] C. Wang, A.J. Appleby, F.E. Little, Electrochim. Acta, in press.
[20] T.R. Jow, C.C. Liang, J. Electrochem. Soc. 129 (1982) 1429.
[21] D. Ludecke, Z. Metallkdo. 77 (1986) 278.
[22] A. Anani, S. Crouch-Baker, R.A. Huggins, J. Electrochem. Soc. 135 (1988) 2103.
[23] J. Wolfensine, D. Foster, J. Read, W.K. Behl, W. Lueck, J. Power Sources 87 (2000) 1.
[24] I.A. Courtney, W.R. McKinnon, J.R. Dahn, J. Electrochem. Soc. 146 (1999) 59.